Check for updates

Photoconductive arrays on insulating substrates for high-field terahertz generation

DAVID R. BACON,[1,2,4] THOMAS B. GILL,[1] MARK ROSAMOND,[1] ANDREW D. BURNETT,[3] ANIELA DUNN,[3] LIANHE LI,[1] EDMUND H. LINFIELD,[1] A. G. DAVIES,[1] PAUL DEAN,[1] AND JOSHUA R. FREEMAN[1,5]

[1]*School of Electronic and Electrical Engineering, University of Leeds, Woodhouse Lane, Leeds LS9 2JT, United Kingdom*
[2]*Femtosecond Spectroscopy Unit, Okinawa Institute of Science and Technology Graduate University, 1919-1 Tancha, Onna-son, Kunigami, Okinawa 904-495, Japan*
[3]*School of Chemistry, University of Leeds, Woodhouse Lane, Leeds LS9 2JT, United Kingdom*
[4]*david.bacon@oist.jp*
[5]*j.r.freeman@leeds.ac.uk*

Abstract: We report on the design, fabrication and characterisation of large-area photoconductive THz array structures, consisting of a thin LT-GaAs active region transferred to an insulating substrate using a wafer-scale bonding process. The electrically insulating, transparent substrate reduces the parasitic currents in the devices, allowing peak THz-fields as high as $120\,\mathrm{kV\,cm^{-1}}$ to be generated over a bandwidth >5 THz. These results are achieved using lower pulse energies than demanded by conventional photoconductive arrays and other popular methods of generating high-field THz radiation. Two device sizes are fully characterised and the emission properties are compared to generation by optical rectification in ZnTe. The device can be operated in an optically saturated regime in order to suppress laser noise.

1. Introduction

In recent years, the development of table-top amplified laser sources together with the use of high-energy synchrotron facilities, has led to the emergence of new sources of intense THz radiation. Techniques such as optical-pump-intense-THz-probe (OPITP) [1], THz-pump-THz-probe (TPTP) [2] and THz-pump-optical-probe (TPOP) [3] have all been employed to investigate the non-linear THz properties of various materials including GaAs [1,4,5], graphene [3,6,7] and n-doped InGaAs [2,8]. Applications of high field pulses are diverse, and include the ability to ionize Rydberg states in Na atoms [9,10], to vary superconductivity through the breakup of cooper pairs in $YBa_2Cu_3O_7$ [11] and to manipulate and control electron spin in antiferromagnets [12].

The high THz fields, which are key to these studies, have typically been generated in accelerator-based synchrotron facilities [13], or on table-top systems through optical rectification (OR) [14], two-colour air-plasma [15,16] or, to a lesser extent, using large-area photoconductive antennas (LAPCA) [17–19]. OR has been shown to work effectively in non-linear crystals [20,21] such as ZnTe. The highest efficiencies are seen in $LiNbO_3$, where a tilted wavefront pumping technique is required [22], but efficiencies >1% are possible [23,24]. Organic crystals such as DAST and OH1 also show promise despite proving difficult to grow over large areas [25,26]. However, there are disadvantages to using OR, which can include the high cost and fragility of the crystals, phase matching constraints, and poor beam quality [20]. Furthermore, the necessity for high optical

pulse energies in the mJ range and complicated optical setups can prove difficult in multi-beam tabletop experiments such as TPTP.

Unlike OR, which is a second order non-linear optical process, photoconductive (PC) emission produces THz radiation through the generation and acceleration of electron-hole pairs in semiconducting materials [17,27,28]. This has several advantages over OR including a bias-controllable output field and electrically switchable polarisation [29]. When optically exciting at 800 nm, one of the most heavily researched materials for use in PC switches is low-temperature-grown gallium arsenide (LT-GaAs), which incorporates excess arsenic trapping sites to enable a very short carrier lifetime, typically $\sim$300 fs [30,31]. It can also be engineered to exhibit very high breakdown fields (500 kV cm^{-1}) [32,33] and high resistivity comparable with that of semi-insulating (SI)-GaAs [34] or silicon-on-sapphire [28]. LT-GaAs is typically fabricated by single crystal growth by molecular beam epitaxy (MBE), either directly on a SI-GaAs wafer or on a thin insulating layer of AlGaAs to separate the LT- and SI-GaAs materials. We have recently demonstrated that by removing the LT-GaAs film from its SI-GaAs substrate and bonding it to *z*-cut quartz, a significant increase in output THz field can be achieved. This is because the parasitic current channel through the SI-GaAs substrate is removed, thereby eliminating a significant source of heating in the device and allowing both higher optical powers and electrical biases to be applied before saturation and device failure [35].

The high efficiency of PC emitters has motivated the development of LAPCAs based on SI-GaAs and LT-GaAs over the past 20 years, however there have been few examples of semiconductor-based LAPCAs used in non-linear THz experiments, where fields of $>$100 kV cm^{-1} are often required. In many cases, the THz field is limited by multiple saturation and localised screening effects [36,37], device heating, relatively low breakdown fields of the material [32] and high optical noise that is typical of amplified laser systems [38]. One effective means of delaying optical saturation is by increasing the active region area. This is typically achieved by either increasing the gap width of a single antenna to several centimeters [38–40] or employing an interdigitated electrode structure design [19,41]. In the case of a single large gap, the higher voltages required to bias the device are known to add significant electrical noise to the detected pulse and thus limit its use in applications. With interdigitated structures lower voltages are required as the geometry typically consists of a single anode and cathode, each connected to multiple parallel electrodes. By illuminating every other electrode gap to avoid destructive interference, active regions up to several cm-wide can be excited simultaneously. Several examples of LAPCA structures using LT-GaAs and SI-GaAs as the active material have been reported [42–46], all of which were designed with relatively small PC gaps ($<$10 μm). While smaller gaps allow for lower bias voltages and are typically more efficient, they can also complicate the fabrication process and typically result in earlier optical saturation, as small gap devices have been shown to suffer more from space-charge screening effects [36,47].

In this work, we use LT-GaAs-on-insulator PC material to fabricate scalable large-area interdigitated array structures with semi-wide gaps in order to generate high THz output fields. However, rather than using Van der Waals bonds as we previously demonstrated in Ref. [35], here the LT-GaAs is wafer-bonded to the insulating substrate with the aid of benzocyclobutene (BCB) [48–50]. This technique, developed for this purpose, ensures a much more uniform and reliable bond between the LT-GaAs and substrate over a larger area. This allows us to use the costly MBE-grown material efficiently, as the majority of bonded LT-GaAs can be used to generate THz radiation. The choice of insulating substrate was dependent on the device area. Smaller devices were fabricated on *z*-cut quartz whereas, for devices larger than 1 cm^2, sapphire was chosen, because of the closely matched thermal expansion coefficients of sapphire and GaAs. Similar to *z*-cut quartz, sapphire is also chemically inert, optically transparent and highly insulating. These properties are crucial when working with an amplified laser system as the high pulse energies can easily result in the thermal breakdown of devices [51]. To demonstrate the scalability

and versatility of this fabrication technique, two devices of different size and design have been fabricated, tested and compared directly with the emission characteristics of a 2-mm-thick <110> cut ZnTe crystal. We demonstrate that by employing a through-substrate-excitation technique, the larger of the two devices is able to generate a maximum output THz field of $120 \, \text{kV} \, \text{cm}^{-1}$ using an optical pulse energy of 0.6 mJ. Not only does this represent a significant improvement over previously published LT-GaAs [46] and SI-GaAs [43,45] array designs, it demonstrates comparable fields to those achieved with ZnSe-based devices [47,52], while requiring an order of magnitude lower optical energy and two orders of magnitude lower electrical bias voltage.

2. Fabrication

The 2-μm-thick LT-GaAs layers used in this study were grown at ~290 °C using MBE, with a 400-nm-thick sacrificial $Al_{0.7}Ga_{0.3}As$ layer to separate the active layer from the SI-GaAs substrate. After the wafers were scribed and diced into samples matching the desired active area, each sample was annealed for 15-min at 550 °C to increase the LT-GaAs resistivity [53]. The fabrication steps are outlined in Fig. 1. In order to bond the LT-GaAs to the insulating substrate, a 300-nm-thick layer of BCB (cyclotene 4024-40) thinned with mesitylene (2:1 by weight) was spun onto the substrate [48]. A thin layer of BCB was important to ensure effective heat transfer between the two materials, as well as to avoid optical absorption. The two surfaces were brought together inside the wafer-bonder chamber (AML AWB aligner) under vacuum and heated. The baking time and temperature are critical to the curing process of the BCB, to ensure chemical resistivity and the eventual bond strength [48]. While sapphire-mounted devices can be bonded at 250 °C for 1 hour, to reach the same bond quality with *z*-cut quartz, a lower temperature and longer duration was required owing to the large thermal expansion coefficient mismatch between quartz and GaAs. In both cases, a maximum pressure of $500 \, \text{N} \, \text{cm}^{-2}$ was exerted on the sample. Once bonded, the SI-GaAs substrate was chemically-mechanically polished to ~30 μm thick. The remaining portion of the substrate was removed using a 5:1 ratio of citric acid ($C_6H_8O_7$:H_2O, 1:1 by weight) and H_2O_2. This etch is known to provide excellent selectivity between the SI-GaAs and AlGaAs layers [54,55]. The AlGaAs was then removed using buffered HF.
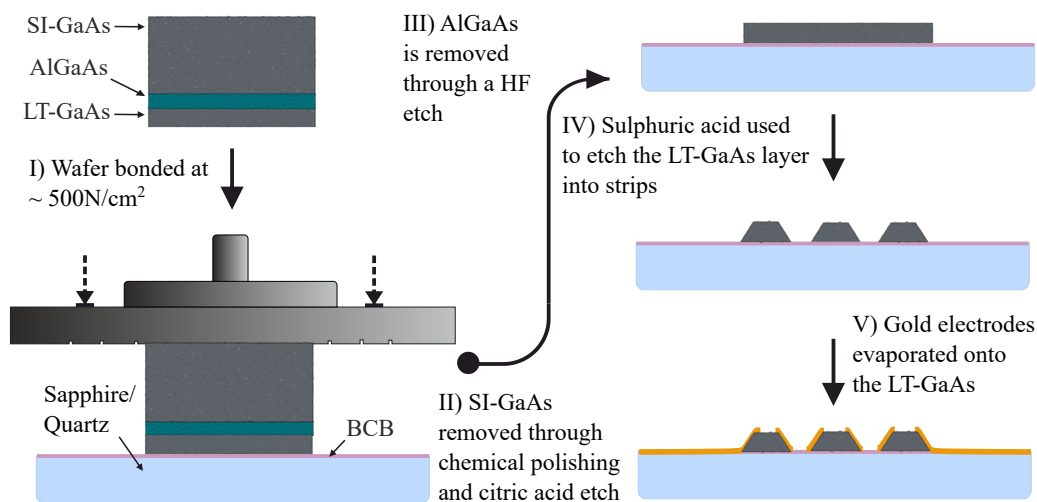
Fig. 1. A simplified flow diagram illustrating the major steps of the fabrication process of quartz/sapphire mounted photoconductive array structures.

To avoid destructive interference of the generated THz field, it is important to only generate the transient current in every-other gap of the interdigitated electrodes. Because of the optically transparent substrate, we are able to simply remove the LT-GaAs layer in every-other gap [44]. This has the significant advantage, compared to conventional photoconductive arrays, of avoiding dark currents and breakdown in the insulators that are required for those devices when the photoconductive SI-GaAs substrate is present. It also simplifies the fabrication process as an extra optical block is not required. The LT-GaAs layer is patterned using a positive photoresist (AZ4562) and etched in a dilute sulphuric acid solution ($H_2SO_4:H_2O_2:H_2O$, 1:8:800. vol). The electrical contacts were formed by depositing Ti/Au (15/200 nm) over the entire sample. The lithography described above was then repeated to create an etch mask for the potassium iodide and buffered HF that were used to etch through the gold and titanium respectively, to form the electrodes. Annotated optical microscope images of the smaller quartz-mounted device (3x3 mm/device A) and larger sapphire-mounted sample (18x18 mm/device B) are shown in Fig. 2(a) and (b) respectively. For the larger of the two devices, the ends of electrodes were intentionally rounded to avoid electric field concentration.
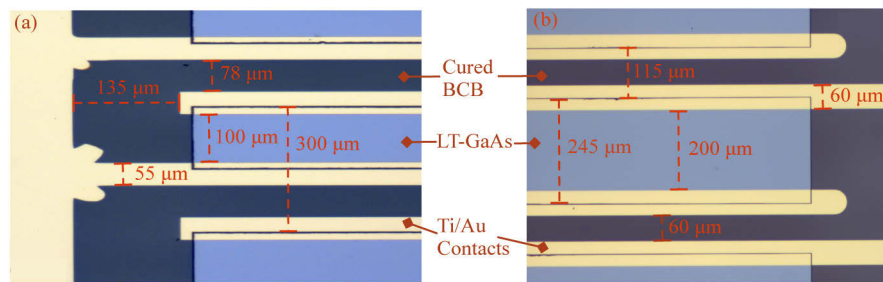
Fig. 2. Annotated microscopy images of two complete PC interdigitated arrays. (a) is a quartz-mounted device with a 9 mm^2 active region, containing 10 individual PC gaps, each 3-mm-long and 100-μm-wide. (b) is a sapphire-mounted device with a 324 mm^2 active region, and 46 separate PC gaps, each 200-μm-wide and 18-mm-long.

3. Experimental characterization of devices

Each device was mounted onto a printed circuit board and positioned in the THz time domain spectroscopy (TDS) system shown in Fig. 3(a), a 2-mm-thick <110> cut ZnTe crystal (10x10 mm) has also be characterised for comparison. They were excited by an amplified laser system (Spitfire PA, Spectra-Physics) providing 40 fs-wide pulses, centred at 800 nm at a 1 kHz repetition rate. The optical beam was split into two parts, the more powerful of which (the 'pump') undergoes 4-times expansion using a reflective telescope geometry ($1/e^2$ beam width ∼40 mm) before being focused through the device using an off-axis parabolic mirror. With this technique the emitted THz radiation is known to follow the NIR excitation beam, leading to both beams having the same focal point. For the LAPCA devices, back-side-illumination was employed such that the NIR beam passes through the quartz/sapphire substrate before optically exciting the LT-GaAs. This avoids any attenuation or dispersion of the THz pulse in the sapphire or quartz. The distance between the parabolic mirror and the emitter was adjusted to fill the active area of the device, while expanded PTFE was used to block the transmitted optical beam. A knife-edge measurement was performed at the THz focal point in the sample position for each emitter and revealed (90/10) spot sizes of ∼1.03±0.08, 0.64±0.04 and 0.63±0.14mm for device A, B and the ZnTe crystal respectively. The first derivative of the knife-edge data taken with device B is shown in Fig. 3(b), together with a Gaussian fit exhibiting a FWHM value of 0.6 mm. Two further off-axis parabolic mirrors were used to collect, collimate and focus the THz radiation onto a 150-μm-thick

<110> cut GaP detection crystal, where the THz field is electro-optically sampled by the weaker 'sampling' beam [56]. This technique uses a pair of balanced photodiodes (Nirvana 2007) to measure the THz induced birefringence of the crystal as a function of time. To enable lock-in detection of the generated THz signal, the photoconductive emitters were electrically biased with a modulation frequency of 125 Hz and a 50 % duty cycle, derived from the 1 kHz repetition rate of the laser. The electrical pulse width used here is relatively long compared with similar studies which require ultra-fast switching to avoid heating issues [38,52]. The removal of the SI-GaAs substrate results in a much higher dark resistance in this case so heating is suppressed. While testing the ZnTe crystal, the pump beam was optically chopped at the same frequency. For all sources the THz beam path was purged in a dry-air environment to avoid water vapour absorption.

Figure 4 shows the THz pulse energy (black) and the optical-to-THz conversion efficiency (red) of each device as a function of optical excitation energy. In order to measure the THz pulse energy, and thus estimate a peak field, a calibrated pyroelectric power-meter (OPHIR RM9-THz) was placed at the focus of the beam in the sample position. THz pulse energy could then be accurately determined by taking into account the laser repetition rate and duty cycle of the electrical modulation, which in this case was set to 50 %. However, owing to the limited sensitivity of the detector, a direct measurement of average power was only possible for device B. For this reason, all sources were fully characterized using electro-optic (EO) sampling. Following that the values for THz power from device A and the ZnTe crystal were calculated from a scaling factor which was determined by comparing the measured power from device B with the integrated FFT power spectrum taken with the same optical excitation and bias conditions. As the same EO detection crystal was employed for all sources, the THz power for any FFT spectrum could be easily retrieved by multiplying its integrated power with this scaling factor and subtracting that power which arrives later in time in the form of system reflections. The accuracy of this method was verified by comparing the calculated and measured power values for different excitation conditions of device B, which showed good agreement with an error of <10%.

The highest output pulse energy in this figure is 102 nJ, achieved using device B with a bias field of 17.5 kV cm^{-1} and optical pulse energy of 0.66 mJ. This represents an increase of three orders of magnitude relative to that achieved using the ZnTe crystal with the same optical pulse energy. The peak optical intensity used here (~1 mJ cm^{-2}) is close to the damage threshold of ZnTe [57,58]. Device A shows similar THz pulse energies to ZnTe, but with optical excitation that is an order of magnitude lower. The quadratic relationship between THz output power and active region area is well established for this type of array structure [59]. However, the increased filling factor of device B, relative to device A (0.5 to 0.33), will also be partly responsible for the large difference in output energy, as a higher percentage of the optical photons incident on the device are used to generate electron-hole pairs. Furthermore, similar structures have reported a direct correlation between the gapsize and generated THz field, mainly attributed to the reduction in the carrier screening effect [47,60]. The shape of the THz pulse energy curves (black) suggests that while optical induced saturation is observed with both devices A and B, the output energy from the ZnTe crystal remains within the linear regime throughout the measurement. Because OR is a second order non-linear optical process, the efficiency should increase linearly, however at high fluences 2-photon absorption and associated free-carrier losses are known to result in a sub-linear increase [21], supported by the data shown in Fig. 4. A maximum efficiency for ZnTe of 5×10^{-7} is achieved, similar to that found by other groups [21]. This is in contrast to devices A and B which exhibit peak efficiencies of 10^{-5} and 3×10^{-4} at optical pulse energies of 2 and 180 μJ respectively. The peak conversion efficiency seen here compares favourably to similar devices published, employing microlens-coupled LT-GaAs-on-SI-GaAs layer structures [46,59]. While it is less than that demonstrated in Ref. [45], this can be explained by the low optical fluence relative to that used here, together with the 5-μm-wide PC gaps in their design,
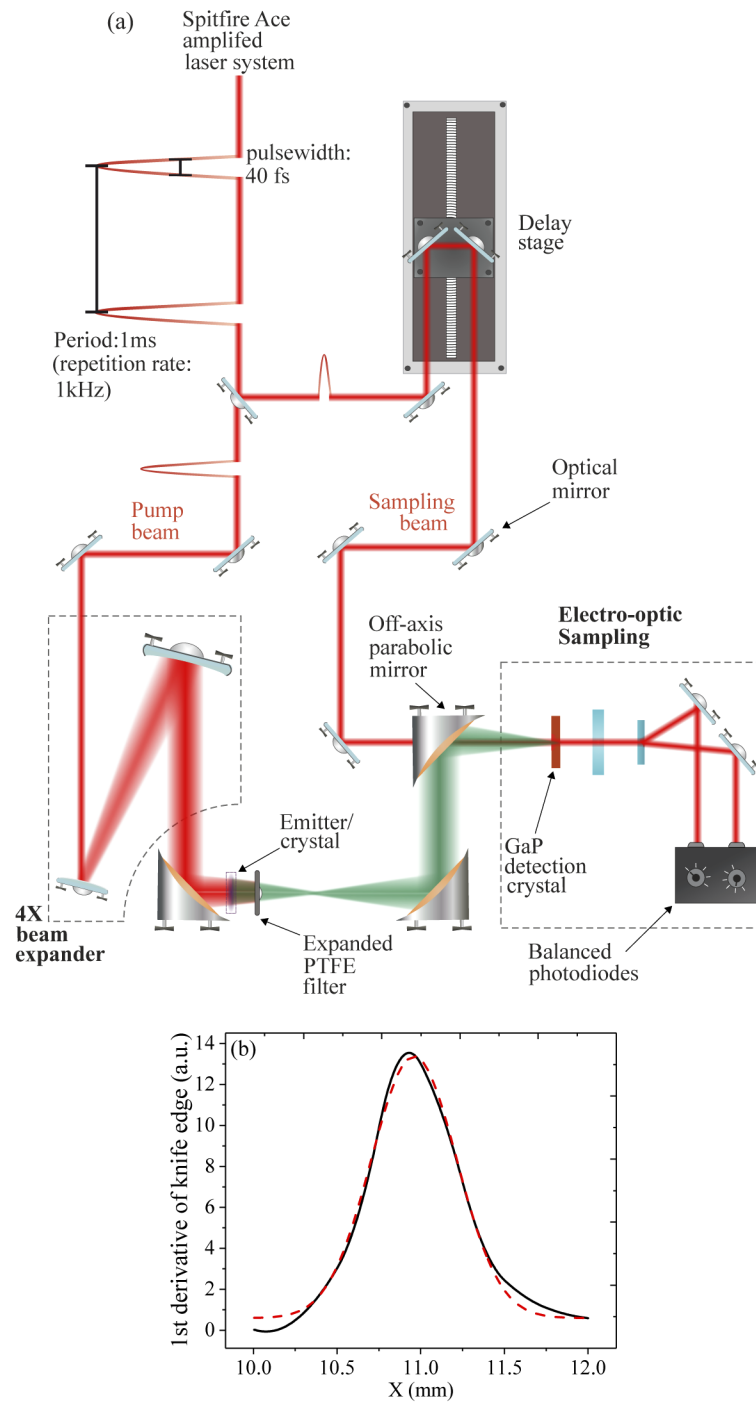
Fig. 3. a) Diagram of the THz-TDS setup used to test the photoconductive array structures. The setup is sourced by an amplified laser system and the focusing of the NIR beam onto the device is performed using an off-axis parabolic mirror. b) First derivative of knife edge measurement data taken at the focus of the THz beam (Device B) and plotted as a function of X, movement of the knife perpendicular to the beam (black line). The data has been fit with a Gaussian function (red dash) with a FWHM value of 0.6 mm.
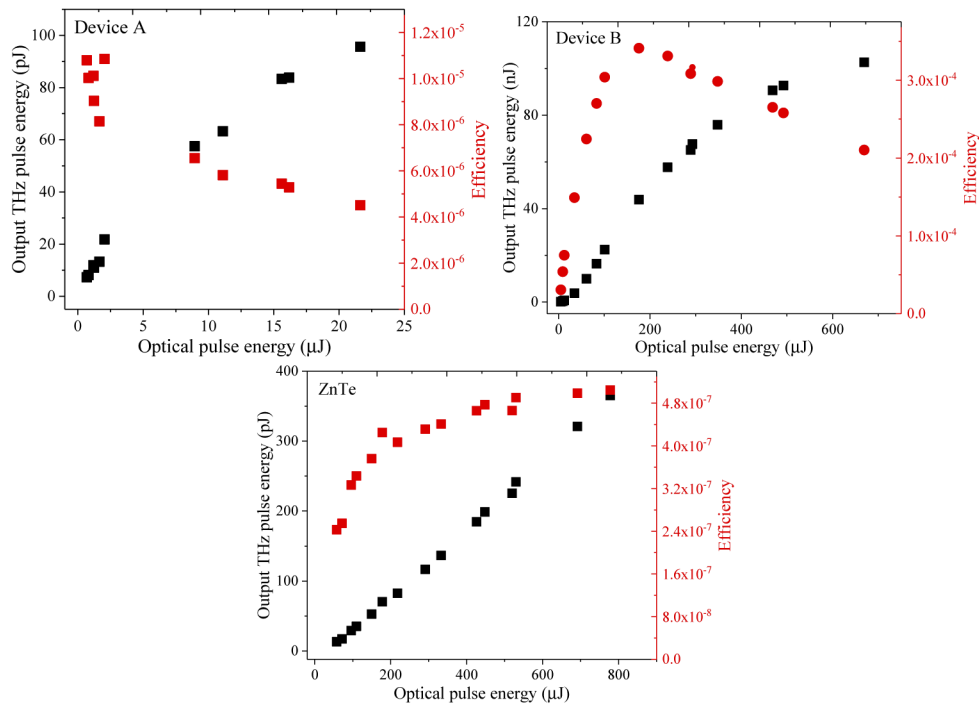
Fig. 4. Output THz pulse energy (black) and efficiency (red) as a function of optical excitation energy for device A ($9\,\mathrm{mm}^2$), device B ($324\,\mathrm{mm}^2$) and a 2-mm-thick ZnTe crystal($100\,\mathrm{mm}^2$). Both photoconductive array structures were electrically biased at $17.5\,\mathrm{kV\,cm}^{-1}$.

allowing a greater packing ratio and 5 times higher bias field than shown here. Interestingly, while device A efficiency decreases as a function of optical excitation energy, device B shows a peak around 180 µJ. This is similar to the response observed in Ref. [59] and is believed to be owing to the non-uniformity of the optical beam intensity across the device which is more prominent for larger devices. A spotsize slightly smaller than the device area, as in Ref. [59], would result in a delayed saturation for the outermost elements of the array and a rise in efficiency as a function of optical fluence. This effect also helps to explain the difference in peak efficiency between device A and B.

Figure 5 shows the dependence of the THz pulse energy (top) and optical-to-THz conversion efficiency (bottom) on applied bias for each device. For this measurement the optical excitation density was set to $190\,\mathrm{µJ\,cm}^{-2}$ for both devices, while the response of device A has been scaled for convenience of plotting. The maximum voltage which could be applied to each device was limited by the breakdown of air between the narrower gaps where the LT-GaAs has been removed. As expected both devices show a quadratic response, with device B exhibiting a maximum THz pulse energy of 113 nJ at the highest tested bias field. While this pulse energy is relatively modest compared to EO crystal generation using tilted lithium niobate, the optical-to-THz conversion efficiency is similar to that typically achieved [14,22], while requiring significantly less optical pulse energy. This makes the device an ideal candidate for use with high repetition amplified systems with lower pulse energy [61]. Furthermore, because the generated THz follows the path of the NIR excitation beam, this assists in the system alignment process and helps to focus the beam tightly to achieve a high THz field. By taking into account the THz pulse energy, the measured spot-size and pulse-width, the peak THz field for device B is $120\,\mathrm{kV\,cm}^{-1}$. This is within 5% of that estimated through EO sampling. This value is still relatively low compared to

that achieved in Ref. [22], where tilted lithium niobate is driven with 4 mJ optical pulse energy. However, the design of this array can be easily scaled to provide higher output power, and does not require a complicated wavefront tilting setup for excitation. Organic crystals can generate similar THz pulse energies to those reported here, but with optical-to-THz conversion efficiencies ~5 times lower [62]. A summary of maximum output values for each source measured here is presented in Table 1 below.
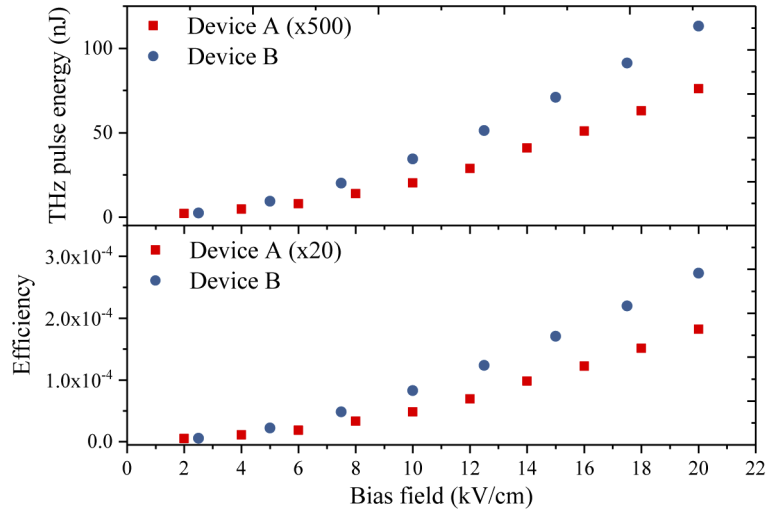
Fig. 5. (Top) THz pulse energy and (Bottom) calculated optical-to-THz conversion efficiency of device A (scaled) and B as a function of bias field across the electrodes. Both devices were excited with an optical density of $190\,\mu\mathrm{J\,cm^{-2}}$

Table 1. Summary of the maximum output values for tested THz sources

Source	Area (mm^2)	THz pulse energy (nJ)	Peak THz field (kV cm^{-1})	Efficiency
ZnTe	100	0.365	8	5×10^{-7}
Device A	9	0.152	2	3×10^{-4}
Device B	324	113	120	1×10^{-5}

The electric field of the THz pulses generated using device B and the ZnTe crystal are shown in Fig. 6 for the same optical fluence ($170\,\mu\mathrm{J\,cm^{-2}}$), with their normalised amplitude spectrum plotted in the inset. This data was recorded with a single scan employing a lock-in amplifier with a time constant set to 100 ms. It is clear from the inset to Fig. 6 that the photoconductive emitter generates a significantly larger bandwidth. The bandwidth of the ZnTe crystal is limited by phase-matching between the optical pump and generated THz beam within the 2-mm-thick crystal, this bandwidth could be increased with a thinner EO crystal, but with a corresponding decrease in generated THz field. From the FFT spectra, values of 32 and 65 dB have been extracted for the peak dynamic range of the ZnTe crystal and device B respectively. It should be noted that a potential drawback of using PC array structures with semi-wide gaps is that higher frequencies, above ~1 THz in this case, can experience interference effects (akin to a diffraction grating) as the wavelengths are less than the array period. This may lead to reduced collection efficiency of the signal at high frequencies. In common with other large array designs [41,43], the peak field in the time-domain is much higher in the first half-cycle compared to the second half-cycle. This has been shown to be an advantage for the non-resonant acceleration of carriers in matter [63], and is believed to be owing to the non-uniformity of the optical phase front across

the device. This is in contrast to that of the ZnTe crystal which shows a full cycle with a distinct trailing oscillation, owing to the limited phase matching of the thick crystal which reduces the potential bandwidth of the output signal. The corresponding data from device A is not shown because of the poor SNR for that device when using the thin GaP EO detection crystal. It should be noted that the dimensions of device A are more suited to higher repetition rate laser systems with lower pulse energies, for which it is predicted a much higher SNR would be achieved.
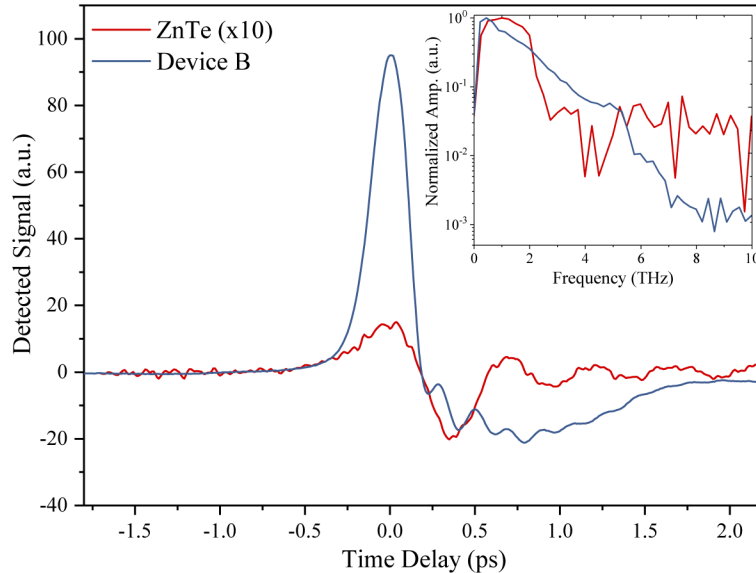
Fig. 6. Main: THz pulse generating using device B (electrical bias field set to $10\,\mathrm{kV\,cm^{-1}}$) and a ZnTe crystal (scaled), both excited with an optical fluence of $170\,\mathrm{\mu J\,cm^{-2}}$ and measured using a 150-μm-thick <110> cut GaP EO detection crystal. Inset: Normalised FFT spectra of the time-domain THz pulses.

Another key advantage of LAPCA devices over other methods of high-field THz generation is that they can be operated in the saturated regime, resulting in a THz pulse that is less dependent on pulse-to-pulse variation or optical power drift over time. This is particularly important when working with low repetition rate amplified systems. In order to demonstrate this, the peak THz field and optical pulse energy have been recorded simultaneously while device B is excited in both the linear and saturated regimes, at 28 and $165\,\mathrm{\mu J\,cm^{-2}}$ respectively. These conditions have been highlighted in the inset of Fig. 7, where the electro-optically sampled peak field has been plotted as a function of optical energy density. The peak THz field for each fluence was then normalised to the mean and plotted as a function of optical signal in the main part of Fig. 7. As expected, when exciting at $28\,\mathrm{\mu J\,cm^{-2}}$ it is clear from the figure that there is a linear relationship between the optical power and THz peak signal. However, as the optical intensity reaches the saturated regime this relationship decouples, effectively reducing the noise in the generated signal. The standard deviation of the THz peak has been calculated for both excitation energies and reveals values of 1.4 % and 3 % of the mean for the high and lower power regimes respectively. This suggests that the THz pulse amplitude noise can be reduced by greater than a factor of 2 by operating the device in the saturation region.
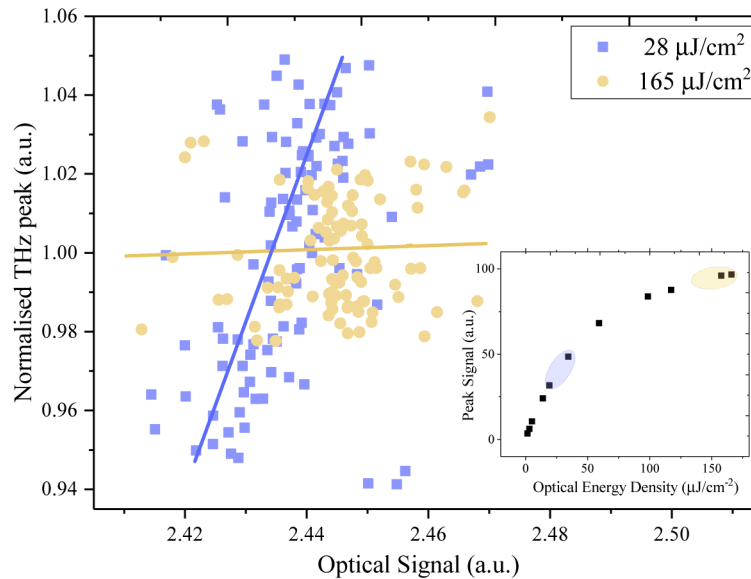
Fig. 7. The normalised THz peak field from 100 separate time-domain scans, plotted as a function of incident optical power. This is plotted for two optical densities of $28\,\mu\mathrm{J\,cm^{-2}}$ (linear regime) and $165\,\mu\mathrm{J\,cm^{-2}}$ (saturated regime) incident on the device. Lines have been added to the scatter graph to guide the eye. Inset: Peak THz field as a function of optical energy density for device B.

4. Conclusion

We have developed large-area photoconductive THz array structures using a thin LT-GaAs active region bonded directly to insulating substrates using a low temperature BCB process. Owing to the electrically insulating optically transparent substrate, as well as the array structure employing semi-wide gaps, the larger of the two devices tested is capable of generating peak THz-fields as high as $120\,\mathrm{kV\,cm^{-1}}$ over a bandwidth greater than 5 THz, without spectral holes. Both structures have been fully characterised as photoconductive emitters and their performance compared to optical rectification in a ZnTe crystal. The THz fields generated from the devices are comparable to tilted lithium niobate and other organic crystals. The advantage of driving the device in a regime of optical saturation has also been demonstrated using the larger of the two photoconductive devices. Finally, we note that the efficiency of the device could be improved by optimisation of the electrode design [47,64,65], or by adding an anti-reflective coating for 800 nm onto the illuminated side of the substrate. Similarly, by depositing a high-κ dielectric material within the inverted gaps where the LT-GaAs has been etched away, higher fields could be applied, enabling an increase in the filling factor. The fabrication procedure detailed here allows for the devices to be scaled, making $1\,\mathrm{MV\,cm^{-1}}$ THz fields generated from this type of device feasible with modest optical pulse energies.

Funding

Acknowledgment

Disclosures

The authors declare no conflicts of interest.

References

1. F. H. Su, F. Blanchard, G. Sharma, L. Razzari, A. Ayesheshim, T. Cocker, L. Titova, T. Ozaki, J.-C. Kieffer, R. Morandotti, M. Reid, and F. A. Hegmann, "Terahertz pulse induced intervalley scattering in photoexcited GaAs," Opt. Express **17**(12), 9620–9629 (2009).
2. F. Blanchard, D. Golde, F. Su, L. Razzari, G. Sharma, R. Morandotti, T. Ozaki, M. Reid, M. Kira, S. W. Koch, and F. A. Hegmann, "Effective mass anisotropy of hot electrons in nonparabolic conduction bands of n-doped InGaAs films using ultrafast terahertz pump-probe techniques," Phys. Rev. Lett. **107**(10), 107401 (2011).
3. S. Tani, F. Blanchard, and K. Tanaka, "Ultrafast carrier dynamics in graphene under a high electric field," Phys. Rev. Lett. **109**(16), 166603 (2012).
4. G. Sharma, I. Al-Naib, H. Hafez, R. Morandotti, D. Cooke, and T. Ozaki, "Carrier density dependence of the nonlinear absorption of intense THz radiation in GaAs," Opt. Express **20**(16), 18016–18024 (2012).
5. R. Jones, D. You, and P. Bucksbaum, "Ionization of rydberg atoms by subpicosecond half-cycle electromagnetic pulses," Phys. Rev. Lett. **70**(9), 1236–1239 (1993).
6. H. Hafez, I. Al-Naib, K. Oguri, Y. Sekine, M. Dignam, A. Ibrahim, D. G. Cooke, S. Tanaka, F. Komori, H. Hibino, and T. Ozaki, "Nonlinear transmission of an intense terahertz field through monolayer graphene," AIP Adv. **4**(11), 117118 (2014).
7. H. A. Hafez, I. Al-Naib, M. M. Dignam, Y. Sekine, K. Oguri, F. Blanchard, D. G. Cooke, S. Tanaka, F. Komori, H. Hibino, and T. Ozaki, "Nonlinear terahertz field-induced carrier dynamics in photoexcited epitaxial monolayer graphene," Phys. Rev. B **91**(3), 035422 (2015).
8. L. Razzari, F. Su, G. Sharma, F. Blanchard, A. Ayesheshim, H.-C. Bandulet, R. Morandotti, J.-C. Kieffer, T. Ozaki, and M. Reid, "Nonlinear ultrafast modulation of the optical absorption of intense few-cycle terahertz pulses in n-doped semiconductors," Phys. Rev. B **79**(19), 193204 (2009).
9. T. J. Bensky, G. Haeffler, and R. R. Jones, "Ionization of Na rydberg atoms by subpicosecond quarter-cycle circularly polarized pulses," Phys. Rev. Lett. **79**(11), 2018–2021 (1997).
10. S. Li and R. Jones, "Ionization of excited atoms by intense single-cycle THz pulses," Phys. Rev. Lett. **112**(14), 143006 (2014).
11. G. L. Dakovski, W.-S. Lee, D. G. Hawthorn, N. Garner, D. Bonn, W. Hardy, R. Liang, M. C. Hoffmann, and J. J. Turner, "Enhanced coherent oscillations in the superconducting state of underdoped $YBa_2Cu_3O_{6+x}$ induced via ultrafast terahertz excitation," Phys. Rev. B **91**(22), 220506 (2015).
12. T. Kampfrath, A. Sell, G. Klatt, A. Pashkin, S. Mährlein, T. Dekorsy, M. Wolf, M. Fiebig, A. Leitenstorfer, and R. Huber, "Coherent terahertz control of antiferromagnetic spin waves," Nat. Photonics **5**(1), 31–34 (2011).
13. H. Hama, M. Yasuda, M. Kawai, F. Hinode, K. Nanbu, and F. Miyahara, "Intense coherent terahertz generation from accelerator-based sources," Nucl. Instrum. Methods Phys. Res., Sect. A **637**(1), S57–S61 (2011).
14. K.-L. Yeh, M. Hoffmann, J. Hebling, and K. A. Nelson, "Generation of 10 μJ ultrashort terahertz pulses by optical rectification," Appl. Phys. Lett. **90**(17), 171121 (2007).
15. T. Oh, Y. Yoo, Y. You, and K. Kim, "Generation of strong terahertz fields exceeding 8 MV/cm at 1 kHz and real-time beam profiling," Appl. Phys. Lett. **105**(4), 041103 (2014).
16. Z. Zhang, Y. Chen, S. Cui, F. He, M. Chen, Z. Zhang, J. Yu, L. Chen, Z. Sheng, and J. Zhang, "Manipulation of polarizations for broadband terahertz waves emitted from laser plasma filaments," Nat. Photonics **12**(9), 554–559 (2018).
17. D. Auston, A. Johnson, P. Smith, and J. Bean, "Picosecond optoelectronic detection, sampling, and correlation measurements in amorphous semiconductors," Appl. Phys. Lett. **37**(4), 371–373 (1980).
18. P. U. Jepsen, R. H. Jacobsen, and S. Keiding, "Generation and detection of terahertz pulses from biased semiconductor antennas," J. Opt. Soc. Am. B **13**(11), 2424–2436 (1996).
19. S. Winnerl, "Scalable microstructured photoconductive terahertz emitters," J. Infrared, Millimeter, Terahertz Waves **33**(4), 431–454 (2012).
20. M. C. Hoffmann and J. A. Fulop, "Intense ultrashort terahertz pulses: generation and applications," J. Phys. D: Appl. Phys. **44**(8), 083001 (2011).
21. T. Löffler, T. Hahn, M. Thomson, F. Jacob, and H. Roskos, "Large-area electro-optic ZnTe terahertz emitters," Opt. Express **13**(14), 5353–5362 (2005).
22. H. Hirori, A. Doi, F. Blanchard, and K. Tanaka, "Single-cycle terahertz pulses with amplitudes exceeding 1 MV/cm generated by optical rectification in $LiNbO_3$," Appl. Phys. Lett. **98**(9), 091106 (2011).

23. S.-W. Huang, E. Granados, W. R. Huang, K.-H. Hong, L. E. Zapata, and F. X. Kärtner, "High conversion efficiency, high energy terahertz pulses by optical rectification in cryogenically cooled lithium niobate," Opt. Lett. **38**(5), 796–798 (2013).

24. W. R. Huang, S.-W. Huang, E. Granados, K. Ravi, K.-H. Hong, L. E. Zapata, and F. X. Kärtner, "Highly efficient terahertz pulse generation by optical rectification in stoichiometric and cryo-cooled congruent lithium niobate," J. Mod. Opt. **62**(18), 1486–1493 (2015).

25. C. P. Hauri, C. Ruchert, C. Vicario, and F. Ardana, "Strong-field single-cycle THz pulses generated in an organic crystal," Appl. Phys. Lett. **99**(16), 161116 (2011).

26. T. Taniuchi, S. Okada, and H. Nakanishi, "Widely tunable terahertz-wave generation in an organic crystal and its spectroscopic application," J. Appl. Phys. **95**(11), 5984–5988 (2004).

27. Y. Shen, P. Upadhya, H. Beere, E. Linfield, A. Davies, I. Gregory, C. Baker, W. Tribe, and M. Evans, "Generation and detection of ultrabroadband terahertz radiation using photoconductive emitters and receivers," Appl. Phys. Lett. **85**(2), 164–166 (2004).

28. A. Warren, N. Katzenellenbogen, D. Grischkowsky, J. Woodall, M. Melloch, and N. Otsuka, "Subpicosecond, freely propagating electromagnetic pulse generation and detection using GaAs:As epilayers," Appl. Phys. Lett. **58**(14), 1512–1514 (1991).

29. C. Mosley, M. Staniforth, A. H. Serrano, E. Pickwell-MacPherson, and J. Lloyd-Hughes, "Scalable interdigitated photoconductive emitters for the electrical modulation of terahertz beams with arbitrary linear polarization," AIP Adv. **9**(4), 045323 (2019).

30. G. Segschneider, T. Dekorsy, H. Kurz, R. Hey, and K. Ploog, "Energy resolved ultrafast relaxation dynamics close to the band edge of low-temperature grown GaAs," Appl. Phys. Lett. **71**(19), 2779–2781 (1997).

31. S. Gupta, J. F. Whitaker, and G. Mourou, "Ultrafast carrier dynamics in III-V semiconductors grown by molecular-beam epitaxy at very low substrate temperatures," IEEE J. Quantum Electron. **28**(10), 2464–2472 (1992).

32. M. Tani, S. Matsuura, K. Sakai, and S.-I. Nakashima, "Emission characteristics of photoconductive antennas based on low-temperature-grown GaAs and semi-insulating GaAs," Appl. Opt. **36**(30), 7853–7859 (1997).

33. J. Luo, H. Thomas, D. Morgan, D. Westwood, and R. Williams, "The electrical breakdown properties of GaAs layers grown by molecular beam epitaxy at low temperature," Semicond. Sci. Technol. **9**(12), 2199–2204 (1994).

34. F. Smith, H. Le, V. Diadiuk, M. Hollis, A. Calawa, S. Gupta, M. Frankel, D. Dykaar, G. Mourou, and T. Hsiang, "Picosecond GaAs-based photoconductive optoelectronic detectors," Appl. Phys. Lett. **54**(10), 890–892 (1989).

35. D. R. Bacon, A. D. Burnett, M. Swithenbank, C. Russell, L. Li, C. D. Wood, J. Cunningham, E. H. Linfield, A. G. Davies, and P. Dean, "Free-space terahertz radiation from a LT-GaAs-on-quartz large-area photoconductive emitter," Opt. Express **24**(23), 26986–26997 (2016).

36. D. S. Kim and D. Citrin, "Coulomb and radiation screening in photoconductive terahertz sources," Appl. Phys. Lett. **88**(16), 161117 (2006).

37. J. T. Darrow, X.-C. Zhang, D. H. Auston, and J. D. Morse, "Saturation properties of large-aperture photoconducting antennas," IEEE J. Quantum Electron. **28**(6), 1607–1616 (1992).

38. E. Budiarto, J. Margolies, S. Jeong, J. Son, and J. Bokor, "High-intensity terahertz pulses at 1-kHz repetition rate," IEEE J. Quantum Electron. **32**(10), 1839–1846 (1996).

39. D. You, R. Jones, P. Bucksbaum, and D. Dykaar, "Generation of high-power sub-single-cycle 500-fs electromagnetic pulses," Opt. Lett. **18**(4), 290–292 (1993).

40. T. Hattori, K. Tukamoto, and H. Nakatsuka, "Time-resolved study of intense terahertz pulses generated by a large-aperture photoconductive antenna," Jpn. J. Appl. Phys. **40**(Part 1, No. 8), 4907–4912 (2001).

41. X. Ropagnol, M. Khorasaninejad, M. Raeiszadeh, S. Safavi-Naeini, M. Bouvier, C. Côté, A. Laramée, M. Reid, M. Gauthier, and T. Ozaki, "Intense THz pulses with large ponderomotive potential generated from large aperture photoconductive antennas," Opt. Express **24**(11), 11299–11311 (2016).

42. A. Dreyhaupt, S. Winnerl, T. Dekorsy, and M. Helm, "High-intensity terahertz radiation from a microstructured large-area photoconductor," Appl. Phys. Lett. **86**(12), 121114 (2005).

43. T. Hattori, K. Egawa, S. Ookuma, and T. Itatani, "Intense terahertz pulses from large-aperture antenna with interdigitated electrodes," Jpn. J. Appl. Phys. **45**(No. 15), L422–L424 (2006).

44. M. Awad, M. Nagel, H. Kurz, J. Herfort, and K. Ploog, "Characterization of low temperature GaAs antenna array terahertz emitters," Appl. Phys. Lett. **91**(18), 181124 (2007).

45. M. Beck, H. Schäfer, G. Klatt, J. Demsar, S. Winnerl, M. Helm, and T. Dekorsy, "Impulsive terahertz radiation with high electric fields from an amplifier-driven large-area photoconductive antenna," Opt. Express **18**(9), 9251–9257 (2010).

46. G. Matthäus, S. Nolte, R. Hohmuth, M. Voitsch, W. Richter, B. Pradarutti, S. Riehemann, G. Notni, and A. Tünnermann, "Large-area microlens emitters for powerful THz emission," Appl. Phys. B **96**(2-3), 233–235 (2009).

47. X. Ropagnol, X. Chai, S. M. Raeis-Zadeh, S. Safavi-Naeini, M. Kirouac-Turmel, M. Bouvier, C.-Y. Côté, M. Reid, M. A. Gauthier, and T. Ozaki, "Influence of gap size on intense THz generation from ZnSe interdigitated large aperture photoconductive antennas," IEEE J. Sel. Top. Quantum Electron. **23**(4), 1–8 (2017).

48. F. Niklaus, R. Kumar, J. McMahon, J. Yu, J.-Q. Lu, T. Cale, and R. Gutmann, "Adhesive wafer bonding using partially cured benzocyclobutene for three-dimensional integration," J. Electrochem. Soc. **153**(4), G291–G295 (2006).

49. F. Niklaus, P. Enoksson, E. Kälvesten, and G. Stemme, "Low-temperature full wafer adhesive bonding," J. Micromech. Microeng. **11**(2), 100–107 (2001).

50. S. Keyvaninia, M. Muneeb, S. Stanković, P. Van Veldhoven, D. Van Thourhout, and G. Roelkens, "Ultra-thin DVS-BCB adhesive bonding of III-V wafers, dies and multiple dies to a patterned silicon-on-insulator substrate," Opt. Mater. Express **3**(1), 35–46 (2013).

51. S. Winnerl, F. Peter, S. Nitsche, A. Dreyhaupt, B. Zimmermann, M. Wagner, H. Schneider, M. Helm, and K. Kohler, "Generation and detection of THz radiation with scalable antennas based on GaAs substrates with different carrier lifetimes," IEEE J. Sel. Top. Quantum Electron. **14**(2), 449–457 (2008).

52. X. Ropagnol, F. Blanchard, T. Ozaki, and M. Reid, "Intense terahertz generation at low frequencies using an interdigitated ZnSe large aperture photoconductive antenna," Appl. Phys. Lett. **103**(16), 161108 (2013).

53. I. S. Gregory, C. Baker, W. Tribe, M. Evans, H. E. Beere, E. H. Linfield, A. Davies, and M. Missous, "High resistivity annealed low-temperature GaAs with 100 fs lifetimes," Appl. Phys. Lett. **83**(20), 4199–4201 (2003).

54. G. C. DeSalvo, W. F. Tseng, and J. Comas, "Etch rates and selectivities of citric acid/hydrogen peroxide on GaAs, $Al_{0.3}Ga_{0.7}As$, $In_{0.2}Ga_{0.8}As$, $In_{0.53}Ga_{0.47}As$, $In_{0.52}Al_{0.48}As$, and InP," J. Electrochem. Soc. **139**(3), 831–835 (1992).

55. A. Kuźmicz, K. Chmielewski, O. Serebrennikova, and J. Muszalski, "Selective etching of GaAs grown over AlAs etch-stop layer in buffered citric acid/H_2O_2 solution," Mater. Sci. Semicond. Process. **63**, 52–57 (2017).

56. Q. Wu and X.-C. Zhang, "Free-space electro-optic sampling of terahertz beams," Appl. Phys. Lett. **67**(24), 3523–3525 (1995).

57. W. Ji, A. Kukaswadia, Z. Feng, S. Tang, and P. Becla, "Nonlinear refraction and optical limiting in bulk ZnTe crystal," J. Cryst. Growth **138**(1-4), 187–190 (1994).

58. H. Lin, B. M. Fischer, and D. Abbott, "Comparative simulation study of ZnTe heating effects in focused THz radiation generation," in *35th International Conference on Infrared, Millimeter, and Terahertz Waves*, (IEEE, 2010), pp. 1–2.

59. G. Matthäus, S. Nolte, R. Hohmuth, M. Voitsch, W. Richter, B. Pradarutti, S. Riehemann, G. Notni, and A. Tünnermann, "Microlens coupled interdigital photoconductive switch," Appl. Phys. Lett. **93**(9), 091110 (2008).

60. L. Hou and W. Shi, "Intense terahertz radiation from μm-gap GaAs photoconductive antenna," J. Phys.: Conf. Ser. **276**, 012208 (2011).

61. R. Paschotta, J. Nilsson, A. C. Tropper, and D. C. Hanna, "Ytterbium-doped fiber amplifiers," IEEE J. Quantum Electron. **33**(7), 1049–1056 (1997).

62. B. Monoszlai, C. Vicario, M. Jazbinsek, and C. Hauri, "High-energy terahertz pulses from organic crystals:DAST and DSTMS pumped at Ti:Sapphire wavelength," Opt. Lett. **38**(23), 5106–5109 (2013).

63. D. Nicoletti and A. Cavalleri, "Nonlinear light-matter interaction at terahertz frequencies," Adv. Opt. Photonics **8**(3), 401–464 (2016).

64. A. Singh, S. Winnerl, J. C. Koenig-Otto, D. R. Stephan, M. Helm, and H. Schneider, "Plasmonic efficiency enhancement at the anode of strip line photoconductive terahertz emitters," Opt. Express **24**(20), 22628–22634 (2016).

65. A. Singh, M. Welsch, S. Winnerl, M. Helm, and H. Schneider, "Improved electrode design for interdigitated large-area photoconductive terahertz emitters," Opt. Express **27**(9), 13108–13115 (2019).